ADVANCED ELECTRONIC MATERIALS

Supporting Information

for *Adv. Electron. Mater.,* DOI: 10.1002/aelm.202200547

Beyond the 2D Field-Effect Charge Transport Paradigm in Molecular Thin-Film Transistors

Emilia Benvenuti, Giuseppe Portale, Marco Brucale, Santiago D. Quiroga, Matteo Baldoni, Roderick C. I. MacKenzie, Francesco Mercuri, Sofia Canola, Fabrizia Negri, Nicolò Lago, Marco Buonomo, Andrea Pollesel, Andrea Cester, Massimo Zambianchi, Manuela Melucci, Michele Muccini, and Stefano Toffanin**

Supporting Information

Beyond the two-dimensional field-effect charge transport paradigm

in molecular thin film transistors

Emilia Benvenuti, Giuseppe Portale, Marco Brucale, Santiago D. Quiroga, Matteo Baldoni, Roderick C. I. MacKenzie, Francesco Mercuri, Sofia Canola, Fabrizia Negri, Nicolò Lago, Marco Buonomo, Andrea Pollesel, Andrea Cester, Massimo Zambianchi, Manuela Melucci, Michele Muccini, Stefano Toffanin**

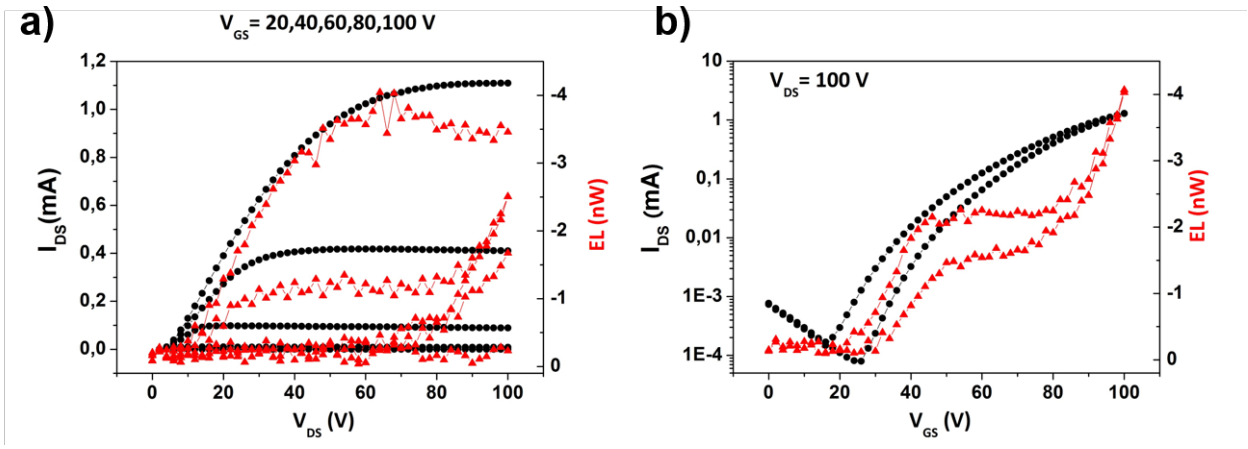

Figure S1. Output (a) and transfer (b) characteristics of NT4N-based OLET (75 nm-thick). Each curve (both forward and backwards) shows drain-source current (I_{DS}, black dots) on the left axis, while the Electroluminescence (EL, red triangles) is plotted on the right axis.

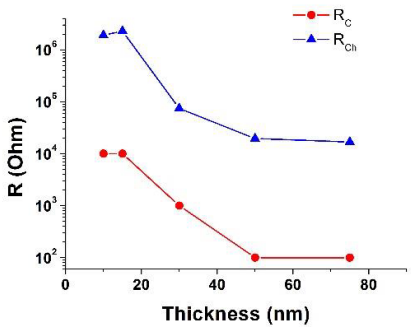

Figure S2. Resistance vs film thickness: comparison between channel resistance R_{Ch} (blue triangles) and contact resistance R_C (red dots); both plotted as a function of organic film thickness.

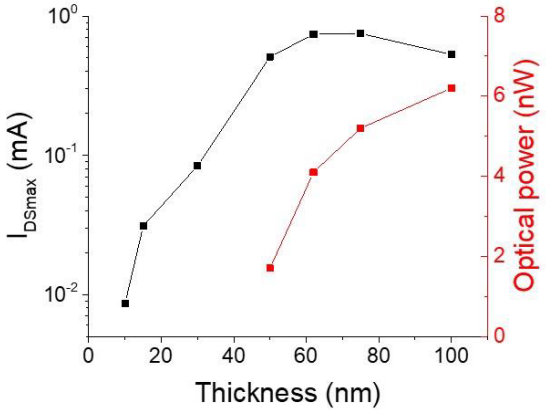

Figure S3. Maximum drain-source current (black squares) and optical power (red squares) as a function of film thickness in NT4N-based OLETs.

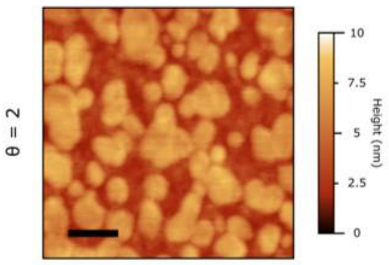

Figure S4. Morphology of a 2nm-thick film of NT4N on PMMA. Scale bar is 100 nm.

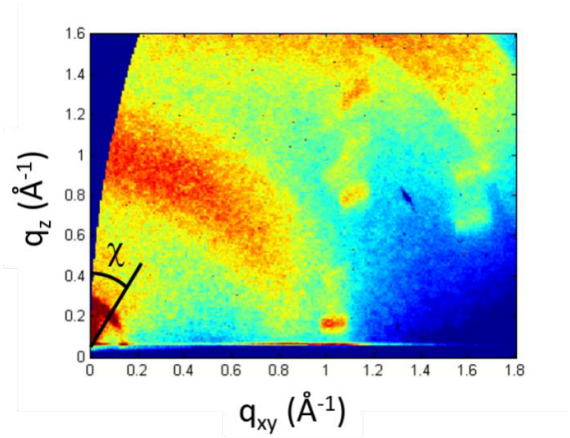

Figure S5. Wedge-corrected GIWAXS image for the 50 nm thick sample.

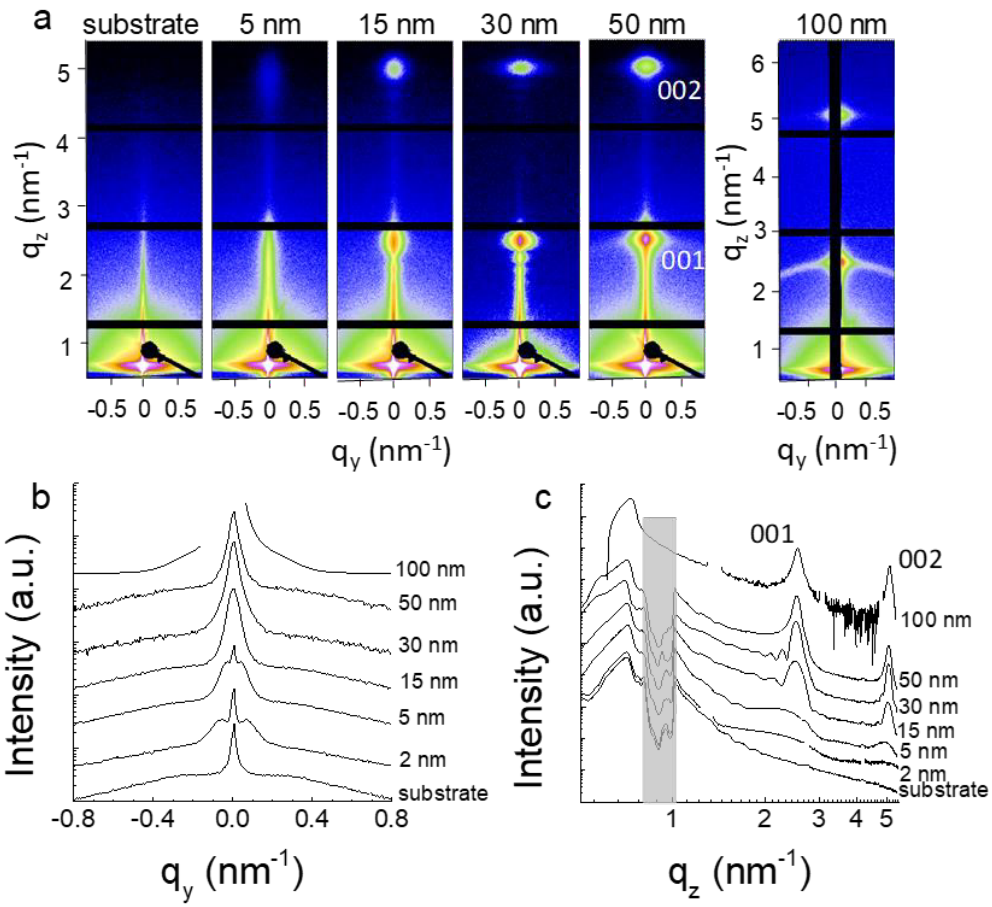

Figure S6 a) Zoomed GISAXS images for the NT4N films at different thicknesses. The angle of incidence used was $\alpha_i = 0.45°$ for all the samples. b) Intensity cuts in the direction parallel to the substrate q_y. c) Intensity cuts along the direction perpendicular to the substrate q_z. The

grey area is the area shadowed by the beamstop. Note that a different detector placement has been used for the 100 nm thick sample.

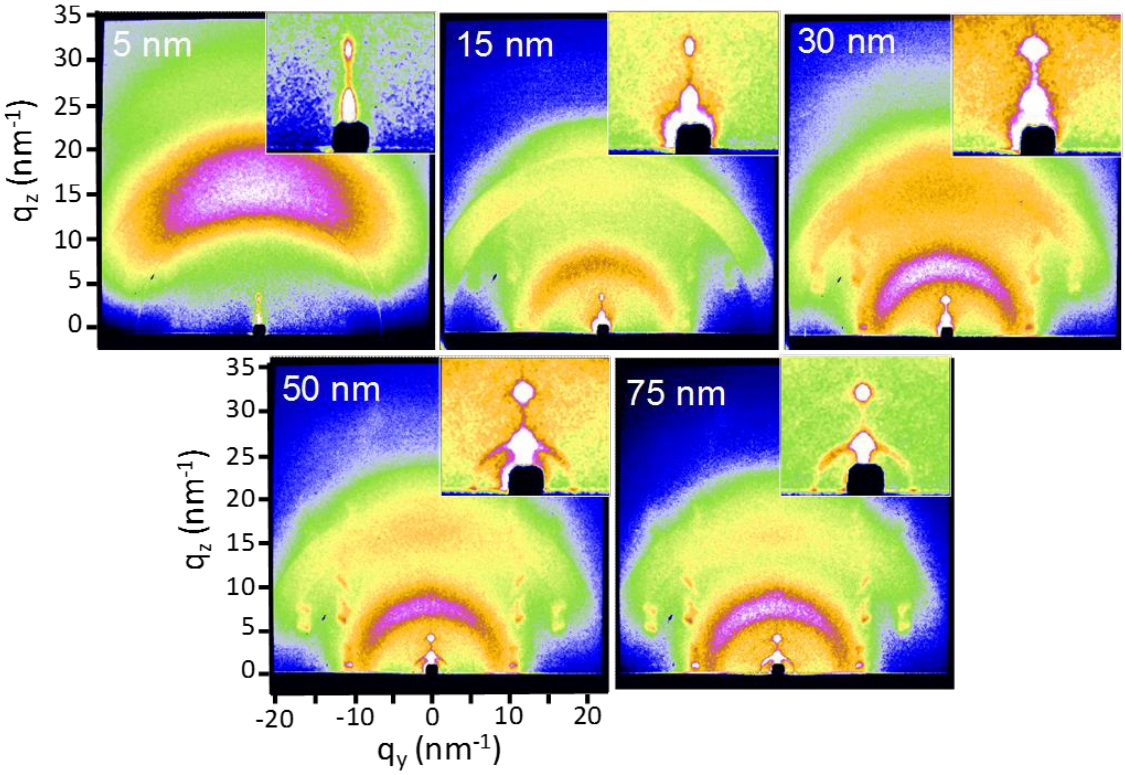

Figure S7. GIWAXS patterns for the NT4N films with different thickness. The insets are zoomed portions relative to the 001 and 002 regions. The angle of incidence used was α_i = 0.15°.

Table S1. Computed TOF charge mobilities for the β crystalline phase of NT4N computed from KMC simulations for an electric field directed along the *a* (μ_a) and *b* (μ_b) crystallographic axes. The highest mobility μ_{max} computed for both carriers n-type and p-type is also reported.

Mobility	μ_a (cm^2/Vs)	μ_b (cm^2/Vs)	μ_a/μ_b*	μ_{max}¬ (cm^2/Vs)
n-type	0.32	0.70	0.46	0.80
p-type	0.01	0.04	0.25	0.04

* Anisotropy ratio between the mobility along *a* axis and the mobility along *b* axis.

¬Maximum computed value of the mobility in the *a,b* plane.

Table S2. Frontier orbital energies and transport gaps for NT4N computed at the B3LYP/6-31G* optimized structures of the neutral systems

Compound	E(HOMO) eV	E(LUMO) eV	E(LUMO+1) eV	ΔE(L/L+1) eV	ΔE(H-L) eV
NT4N	-5.66	-2.87	-2.53	0.35	2.78

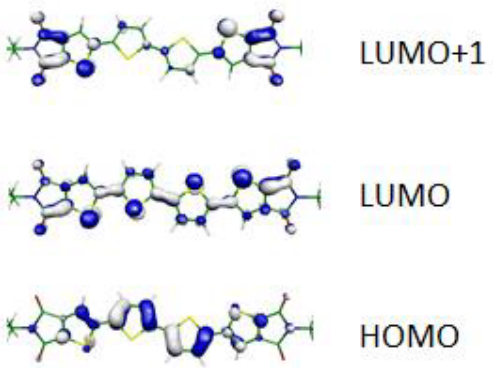

Figure S8. NT4N frontier orbital shapes at B3LYP/6-31G* level of theory

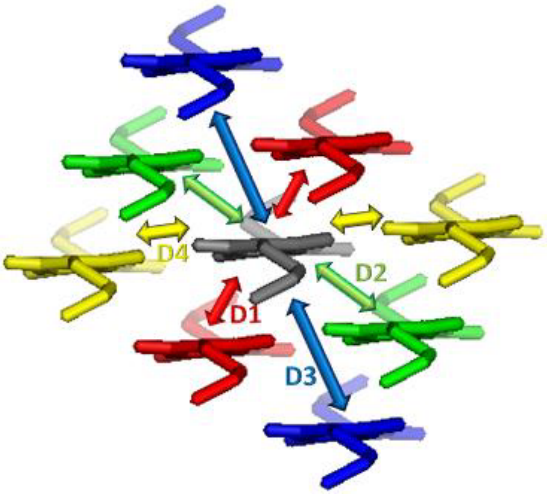

Figure S9. Schematic view of the hopping pathways from the central grey molecule to the nearest neighbors in the *ab* crystallographic plane of the β phase of NT4T. The available pathways are labelled with increasing numbers (D1 to D4) for increasingly larger intermolecular distances between the centers of mass of the molecules forming the dimers.

Table S3. Computed electronic couplings (B3LYP/6-31G* level of theory) for n-type and p-type charge transport for the phase β of NT4N

Dimer label	Dist. / Å	V_{ij}^{HOMO} / meV	V_{ij}^{LUMO} / meV	V_{ij}^{LUMO+1} / meV
D1	5.1270	6	22	30
D2	5.5260	10	40	29
D3	7.2841	0	1	1
D4	7.7838	3	24	10

Table S4. Intramolecular reorganization energy computed with the adiabatic potential (AP) method, at B3LYP/6-31G* level of theory, for n-type and p-type charge transport: $\lambda_i^{n\,(AP)}$ and $\lambda_i^{c\,(AP)}$ are the contributions from the neutral and charged states, respectively, to the total AP reorganization energy λ_i^{AP}

Compound	λ_i^{AP} / eV	$\lambda_i^{n\,(AP)}$ / eV	$\lambda_i^{c\,(AP)}$ / eV
n-type NT4N	0.363	0.163	0.200
p-type NT4N	0.340	0.148	0.192

Table S5. Effective frequency ω_{eff} and associated Huang-Rhys factor S_{eff} employed in the KMC simulations

Compound	ω_{eff} / cm^{-1} [a]	S_{eff} [a]	λ_i^{ref} / eV [a]	λ_{class} /eV [b]	λ_{class}^{tot} /eV [c]
n-type NT4N	1070	2.070	0.274	0.089	0.099
p-type NT4N	985	2.002	0.245	0.095	0.109

[a] Refined values, considering only frequencies above 150 cm^{-1}. [b] Contributions to classical reorganization energy from intramolecular classical vibrations. [c] Total classical reorganization energy, adding 0.01 eV to λ_{class}, the contribution of external reorganization energy.

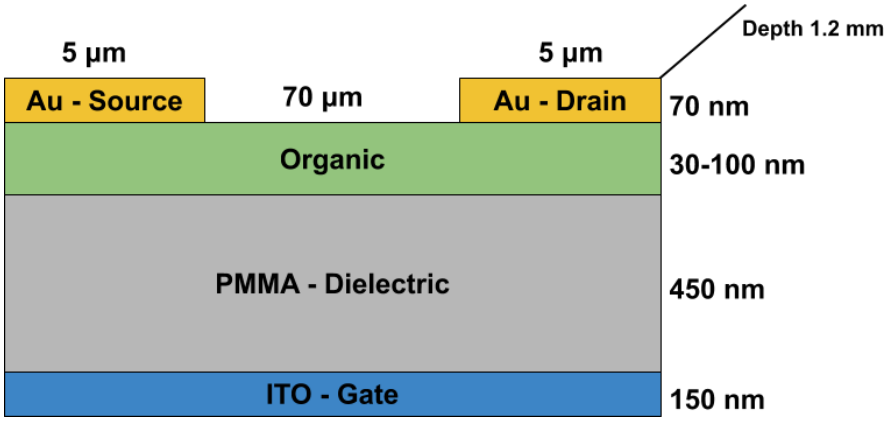

Figure S10. Schematic representation of the device architecture used throughout all the full-scale drift-diffusion simulations.

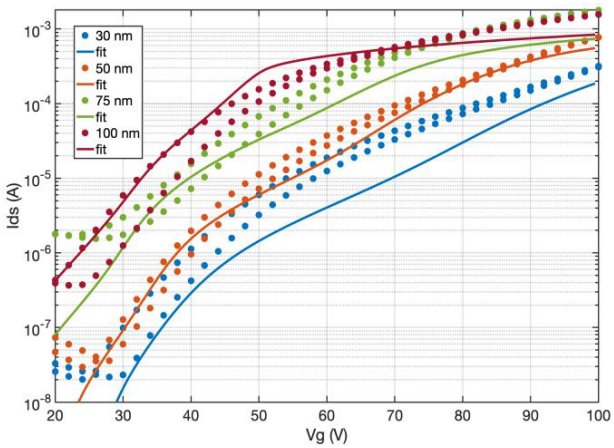

Figure S11. Fit of the model to the experimental saturation transfer curves for some representative NT4N devices of increasing thickness.

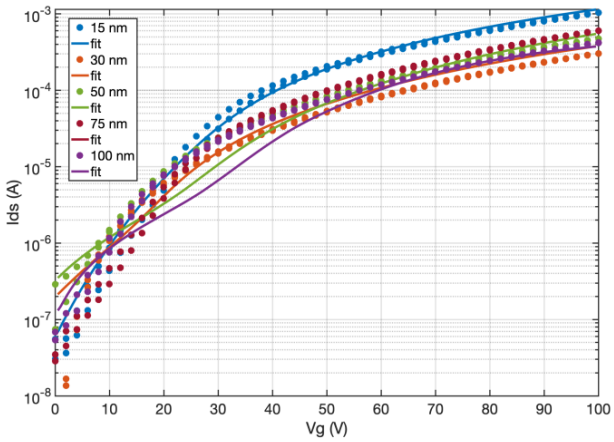

Figure S12. Fit of the model to the experimental saturation transfer characteristics for devices fabricated using PTCDI-C13 as a semiconducting active layer. For details about the fabrication of PTCDI-C13 devices, see Ref. [1].

Table S6. Computational parameters used in the simulations of NT4N-based devices. The thickness-dependent parameters are reported in Table S7.

	NT4N	Dipole layer 0	Dipole layer 1	PMMA
Trap density ($m^{-3}eV^{-1}$)	See Table S7	1.00E+10	1.00E+10	1.00E+10
Tail slope (eV)	0.08	0.04	0.04	0.04
Charge carrier mobility ($m^2V^{-1}s^{-1}$)	1.00E-02	1.00E-15	1.00E-15	1.00E-15
Relative permittivity (au)	6	2	2	2
Number of traps (bands)	2	2	2	2
Free carrier to trapped carrier (m^{-2})	1.00E-19	1.00E-20	1.00E-20	1.00E-20

Trapped carrier to free carrier (m^{-2})	1.00E-18	1.00E-17	1.00E-17	1.00E-17
Effective density of free electron states @300K (m^{-3})	5.00E+25	5.00E+25	5.00E+25	5.00E+25
Xi (eV)	2	1.6	1.6	1.6
Eg (eV)	2	2.4	2.4	2.4
Doping starts (m^{-3})	0	See Table S7	0	0
Doping stop (m^{-3})	0	See Table S7	0	0
Doping dipole contact/NT4N (m^{-3})	3.00E+23			

Table S7. Thickness-dependent Computational parameters used in the simulations of NT4N-based devices.

Thickness (nm)	Trap density (m^{-3})	NT4N/PMMA dipole doping (m^{-3})
30	4.50E+25	-2.70E+24
50	3.00E+25	-2.00E+24
75	2.00E+25	-1.40E+24
100	1.00E+25	-1.20E+24

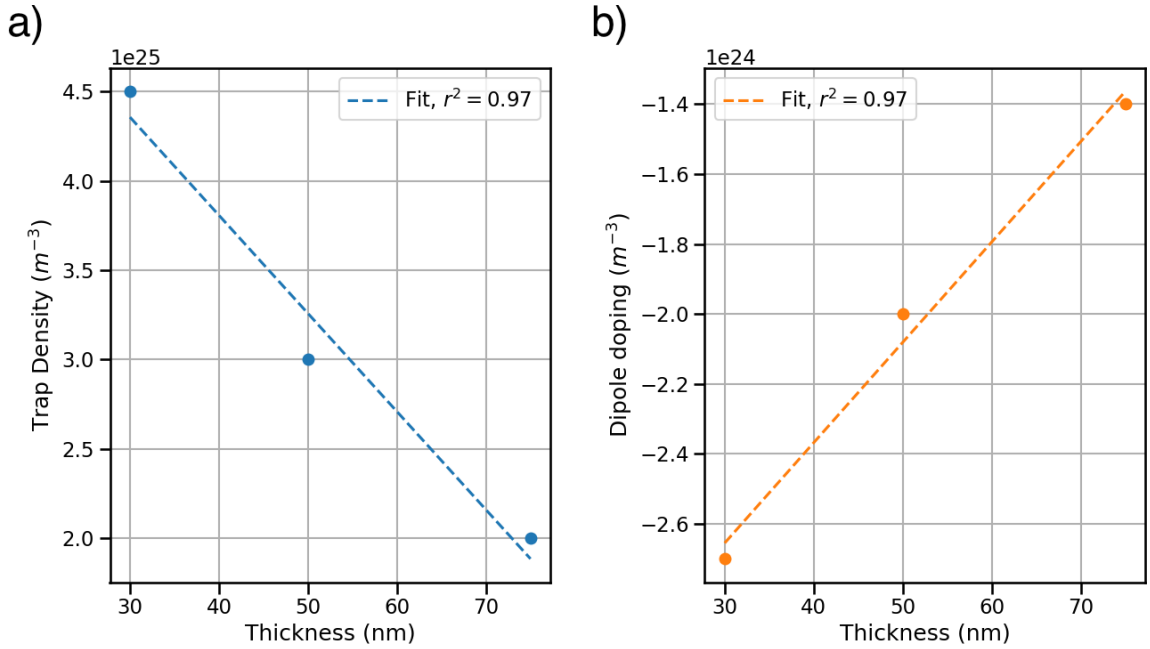

Figure S13. Correlation between the model thickness and the values of the thickness-dependent parameters: trap density (a), and dipole doping. Please bear in mind that, for technical reasons, the sign of the dipole doping is the opposite of the actual dipole concentration.

Table S8. Computational parameters used in the simulations of PTCDI-C13-based devices. The thickness-dependent parameters are reported in table S9.

	P13	Dipole layer 0	Dipole layer 1	PMMA
Electron trap density ($m^{-3}eV^{-1}$)	2.00E+25	1.00E+10	1.00E+10	1.00E+10
Electron tail slope (eV)	0.08	0.04	0.04	0.04
Electron mobility ($m^2V^{-1}s^{-1}$)	See Table S9	1.00E-15	1.00E-15	1.00E-15
Relative permittivity (au)	6	2	2	2

Number of traps (bands)	2	2	2	2
Free carrier to trapped carrier (m^{-2})	1.00E-19	1.00E-20	1.00E-20	1.00E-20
Trapped carrier to free carrier (m^{-2})	1.00E-18	1.00E-17	1.00E-17	1.00E-17
Effective density of free electron states @300K (m^{-3})	5.00E+25	5.00E+25	5.00E+25	5.00E+25
Xi (eV)	2	1.6	1.6	1.6
Eg (eV)	2	2.4	2.4	2.4
Doping starts (m^{-3})	0	-1.40E+23	0	0
Doping stop (m^{-3})	0	-1.40E+23	0	0
Doping dipole contact/NT4N (m^{-3})	See Table S9			

Table S9. Thickness-dependent computational parameters used in the simulations of PTCDI-C13-based devices.

Thickness (nm)	Mobility ($m^2V^{-1}s^{-1}$)	Doping dipole contact/P13 (m^{-3})
30	5.00E-04	6.31E+23
50	1.00E-03	3.98E+23
75	1.40E-03	2.00E+23
100	1.26E-03	2.00E+23

References

[1] M. Natali, M. Prosa, A. Longo, M. Brucale, F. Mercuri, M. Buonomo, N. Lago, E. Benvenuti, F. Prescimone, C. Bettini, A. Cester, M. Melucci, M. Muccini, S. Toffanin, *ACS Applied Materials & Interfaces*, 2020, **12** (27), 30616-30626